Probing the Turbulence Dissipation Range and Magnetic Field Strengths in Molecular Clouds. II. Directly Probing the Ion–neutral Decoupling Scale

Kwok Sun Tang[1] , Hua-Bai Li[1] , and Wing-Kit Lee[2]
[1] Department of Physics, The Chinese University of Hong Kong, NT., Hong Kong SAR; kwoksun2@illinois.edu, hbli@cuhk.edu.hk
[2] Institute of Astronomy and Astrophysics, Academia Sinica, P.O. Box 23-141, Taipei 10617, Taiwan
Received 2018 January 21; revised 2018 June 4; accepted 2018 June 6; published 2018 July 20

Abstract

The line width of ions has been observed to be systematically narrower than that of the coexisting neutrals in molecular clouds and been interpreted as the signature of the decoupling of the neutral turbulence from magnetic fields in partially ionized medium. As a sequel of Li & Houde, here we present further observational evidence that supports these earlier proposals with the velocity coordinate spectrum analysis. We recover the turbulent energy spectra of HCN and HCO^+ $(4 - 3)$ in a starless molecular cloud in NGC 6334 where magnetic fields play a dynamically important role. Our analysis showed that the neutral spectrum is consistent with Kolmogorov type ($k^{-5/3}$, where k is the wavenumber), while that of the ions is the same on the large scale, but steeper ($\sim k^{-2}$), for scales smaller than 0.404 pc. We carefully ruled out the possibilities that the spectrum difference can stem from the differences of ion and neutral optical depth and hyperfine structure.

Key words: ISM: clouds – magnetohydrodynamics (MHD) – magnetic fields – turbulence

1. Introduction

Magnetic fields (*B*-fields) are ubiquitous in the Milky Way and are believed to play various important roles in converting galactic gas into stars (for a recent review, see Li et al. 2014). In most analyses and numerical simulations, gas and *B*-fields are treated as perfectly coupled. This is a fairly good approximation when large scales are considered. However, at smaller scales, the decoupling between gas flows and *B*-fields, also known as ambipolar diffusion (AD), becomes inevitable. AD is the physical process that describes the relative motion of neutrals and charged particles attached to magnetic field lines in partially ionized media. In the context of star formation, it manifests itself in three different flavors, depending on how the relative motion between the two species is being driven. Gravitationally driven AD, first identified by Mestel & Spitzer (1956) and further developed by Mouschovias (1979) and Nakano et al. (2002), corresponds to the process of how neutrals drift through the charged particles due to their self-gravity, and how it consequently leads to the increase in the mass-to-magnetic-flux ratio of the molecular clouds. Magnetically driven AD (Mouschovias 1987; Mouschovias et al. 2011) is concerned with the process of how magnetohydrodynamic (MHD) waves are damped due to the imperfect coupling between neutrals and charged particles in non-turbulent media. It has been proposed to facilitate the removal of turbulent support against gravity and possibly initiate the fragmentation of molecular cloud cores (Mouschovias 1987, 1991; Mouschovias et al. 2011). Turbulence-driven AD (Li & Houde 2008; Paper I, hereafter, Tilley & Balsara 2010; Burkhart et al. 2015), on the other hand, is concerned with the damping of perturbations in *B*-fields in turbulent, partially ionized media. In contrast to the magnetically driven AD, turbulence-driven AD predicts that the turbulent energy/motions in the neutrals would not be damped as soon as the scale at which neutrals decouple from the *B*-fields is reached. Instead, small eddies in the neutrals would be fed by their own turbulent energy cascades, while

the turbulent motions of the ions, which is tied to the *B*-fields, would be dissipated (Paper I).

Despite its importance in various aspect of star formation, to date, there is no direct observational evidence for any types of AD. Observations of AD are either indirect (Paper I, Hezareh et al. 2010, 2014) and/or highly controversial (Crutcher et al. 2010; Mouschovias & Tassis 2010; Li et al. 2014; Tritsis et al. 2015, Jiang et al. 2018).

In Paper I, we proposed that the line width difference between coexistent ions and neutrals is the manifestation of AD in turbulent medium, and that it can be observed even when the ion–neutral decoupling scale l_{AD} is unresolved by the telescope beam. The rationale behind it is that at scales smaller than l_{AD}, only ions are coupled to the *B*-fields therefore their turbulent motions are inevitably damped in the presence of turbulence-driven AD. The low ionization level of molecular clouds limits the frictional force that acts on the neutrals by ion–neutral collisions. Small-scale motions of neutrals would still be sustained by its own turbulent energy cascade until hydrodynamic viscosity sets in. This claim is further developed and verified by later work such as Li et al. (2010) and Hezareh et al. (2010, 2014). Although this theory readily explained that the line width of HCO^+ is narrower than that of consistent HCN, as first pointed out in Paper I, the relation of turbulent line width and size reported ($\Delta v(k) \propto l^{0.15}$) is consistently shallower than what is expected theoretically for either the Kolmorgorov-type incompressible turbulence $l^{1/3}$ or the observationally favored compressible turbulence $l^{1/2}$ (Heyer & Brunt 2004; McKee & Ostriker 2007), where l is the size of the turbulent eddies considered. Such discrepancies between theory and observations may propagate and eventually affect the determination of the l_{AD}. On one hand, turbulence-driven AD, as we show in the next section, predicts an l_{AD} at sub-parsec scale, the observations seem to support an l_{AD} on the order of $\sim$1–10 mpc (Paper I, Hezareh et al. 2010, 2014). On the other hand, observational biases such as the optical depths and relative abundances of the tracers HCN and HCO^+ are often being criticized as the culprit for the observed line width difference between ions and neutrals.

In this work, we revisit turbulence-driven AD with the velocity coordinate spectrum (VCS) analysis to our observed HCN and HCO$^+$ spectral data cubes. This technique enables modeling the turbulent energy spectra of ions and neutrals, as it can distinguish the underlying turbulence statistics from the contributions of density structures to the spectral lines. This method has been successful in retrieving a statistical description of turbulence in simulation data cubes (Padoan et al. 2009; Chepurnov et al. 2010) and has been applied to various observational data (Padoan et al. 2009; Chepurnov et al. 2015). We present our observation and analysis toward our carefully chosen diffuse molecular cloud in NGC 6334, where B-fields are shown to be dynamically important. We show that neither optical depths nor other intrinsic properties of the tracers are responsible for our results.

We begin with an introduction of turbulence-driven AD and the physics of neutral–ion decoupling, and show that it is a relevant process based on the widely observed scaling relation on the scale of molecular cloud cores in Section 2. Data acquisition and the rationale behind our target selection is presented in Section 3. It is followed by an overview of the VCS analysis (Lazarian & Pogosyan 2006), and the application on NGC 6334 in Sections 4 and 5, respectively. We carefully rule out the factors that might influence our analysis in Section 6. In Section 7, we repeat the same analysis as in Paper I and discuss the origin of the consistently shallower turbulent spectrum presented in these previous works. Finally, the implications of our observation results are discussed in Section 8, followed by a conclusion in the final section.

2. The Physics of Turbulence-driven AD

To understand turbulence-driven AD, we have to first make sense of how turbulent flows, carried mostly by neutrals, are coupled to the B-fields through their collision with ions. The Lorentz force can only be felt by charged species. For neutrals to stay magnetized, collisions between neutrals and ions must be frequent enough for neutrals to capture the motion of ions coupled with the B-fields. The magnetic Reynolds number R_M is a dimensionless parameter that characterizes how well these two species are coupled for turbulent motion of different scales (Paper I; Balsara 1996; Oishi & Mac Low 2006; Tilley & Balsara 2010; Meyer et al. 2014). At scales where $R_M \gg 1$, neutrals and ions are well coupled. When R_M is small, neutrals are no longer frozen into the B-fields and decouple from the charged species that remain attached to the B-field lines. As a result of the decoupling, ions and neutrals should demonstrate distinct turbulent energy spectra for scales smaller than l_{AD}, as shown in Figure 1(A). The imperfect coupling between the two species induces friction forces on the flows of ions and neutrals and leads to the damping of motions for scales below l_{AD}. Because of the low ionization level in molecular clouds, charged particles are outnumbered by neutral particles by almost ten million times. This means that a charged particle encountering neutral particles is far more likely to occur than a neutral particle bumping into charged particles. Therefore, small-scale motions of ions are expected to be heavily damped in this regime, and this will then prohibit the further cascading of turbulent energy into even smaller length-scale. The frictional force between ions and neutrals is expected to play a role in damping the turbulent energy of neutrals as well, but only a minor one because of the low ionization level (Paper I).

Since neutrals decouple from the B-fields and ions, small-scale turbulent motions in neutrals are still fed on their own turbulent energy cascade and should survive beyond the decoupling scale. The energy cutoff in neutrals would still predominantly be set by hydrodynamic viscosity for scales smaller than the mean free path of the fluid (Paper I). A rough estimate of the decoupling scale l_{AD} can be made by setting $R_M = 1$:

$$R_M = \frac{l_{AD} V_n}{\beta} = 4\pi m_i m_n \gamma_d \frac{\chi_i n_n^2 l_{AD} V_n}{B^2} = 1,$$

$$l_{AD} = \frac{B^2}{4\pi m_i m_n \gamma_d \chi_i n_n^2 V_n(l_{AD})}, \quad (1)$$

where V_n is the characteristic velocity at the scale of l_{AD}, and β is the effective magnetic diffusivity and is given by $\beta = B^2 / 4\pi m_i m_n \gamma_d \chi_i n_n^2$ (Paper I; Balsara 1996) when AD dominates other non-ideal processes such as the Hall effect and Ohmic dissipation. Here n_n is the number density of neutrals and γ_d represents the drag coefficient arising from the exchange of momentum between ions and neutrals. For typical conditions in molecular clouds, the mean neutral m_n and ion mass m_i are 2.3 and 29 times that of the hydrogen atom, and the drag coefficient γ_d is estimated to be $1.5 \times 10^{-9}\,\mathrm{cm^3\,s^{-1}}$ (Paper I; Mouschovias et al. 2011). χ_i is the ionization fraction of the molecular clouds. Assuming the line width–size relation $\sigma \approx 0.9\,\mathrm{km\,s^{-1}} \left(\frac{1}{1\mathrm{pc}}\right)^{0.5}$ (Heyer & Brunt 2004 and B-field-density scaling relations $B \approx 10\,\mu\mathrm{G}(n/(300\,\mathrm{cm^{-3}}))^{0.65}$ (Crutcher et al. 2010), or $B = 0.19\,\mathrm{mG}(n/(10^3\,\mathrm{cm^{-3}}))^{0.41}$ (Li et al. 2015), one would expect that the decoupling of neutrals from ions should be at work already at sub-parsec scales $l_{AD} \approx 0.13$–$0.41\,\mathrm{pc}$ with a typical cloud core density $n \sim 10^4\,\mathrm{cm^{-3}}$, where the ionization fraction χ_i is approximately 10^{-7} for an assumed cosmic-ray ionization rate of $\approx 10^{-16}\,\mathrm{s^{-1}}$ (Draine 2011).

Note that the decoupling scale l_{AD} we presented here is different from the expression of the Alfvén length scale λ_A derived by Mouschovias (1987) and Mouschovias et al. (2011) based on the linear MHD wave analysis. This stems from the different fundamental assumption taken by these two approaches. Observationally, it is hard to distinguish whether observed line widths are driven by MHD turbulence or MHD waves, however. In the context of molecular clouds, the two length scales approach the same limit, as we show below. The Alfvén length scale λ_A is given by $\pi V_A \tau_{ni}$, where $V_A = \frac{B}{\sqrt{4\pi\rho}}$ is the Alfvén wave speed of the medium, and $\tau_{ni} = 1/n_i \gamma_d$ is the neutral–ion collision timescale. l_{AD} can be written in terms of Alfvén wave speed in the form $\frac{V_A^2 \tau_{ni}}{V}$. Polarimetry observations (e.g., Li et al. 2009, 2015) reveal that the B-field is ordered over a large range of scales in molecular clouds, which is indicative of the trans-Alfvénic nature ($V \approx V_A$) of the medium. The decoupling scale l_{AD} approaches $\approx V_A \tau_{ni}$ when V is on the order V_A, and can therefore be reconciled with the Alfvén length scale λ_A. While it is beyond the scope and capability of this work to distinguish whether an MHD wave or MHD turbulence is a more realistic description of the reality based on spectral line observations, we point our readers to some recent direct two-fluid simulations (Tilley & Balsara 2010; Burkhart et al. 2015) that might shed light on
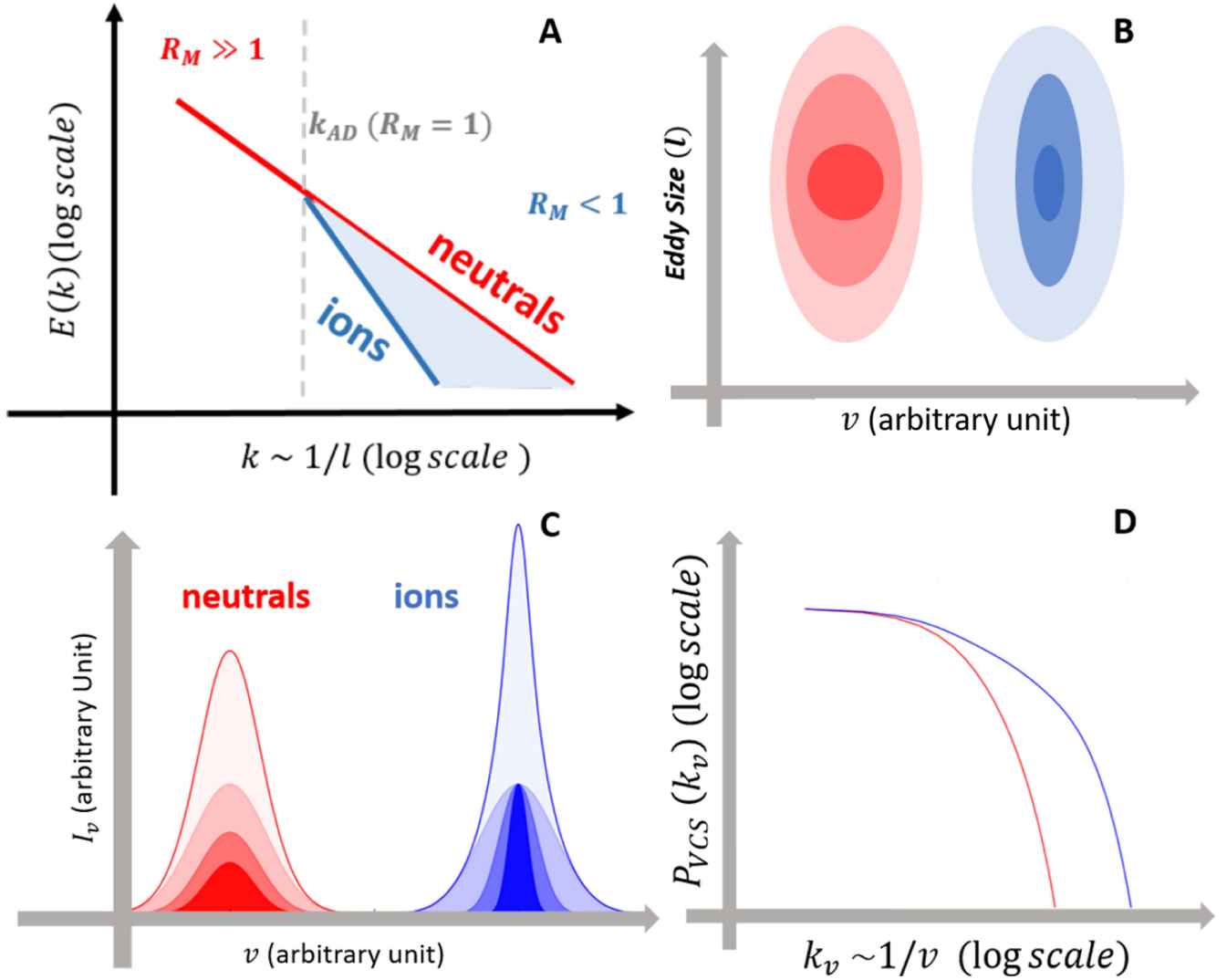
Figure 1. Panel (A): log–log plot of the turbulent velocity spectrum (energy density per unit wavenumber and mass) vs. wavenumber in arbitrary units for demonstrative purposes. The velocity dispersion/line width of the tracers measured at scale L is proportional to the integration of the turbulent energies contributed by all eddies of size smaller than L. The turbulent energy in ions is dissipated steeply for scales smaller than l_{AD} because of turbulence-driven AD. Panel (B): Illustration of mapping turbulent eddies from real space to spectral lines (velocity space) inspired by Lazarian (2009). In real space, there are three eddies of same density, but different velocity dispersion. The larger the velocity dispersion of the eddies, the larger the extent of it in the velocity space. Here the largest eddy of these two species shares the same velocity dispersion. Because of the difference in the turbulent energy spectra (Panel (A)), the energy carried by the small ion eddies decreases faster with scale. The spread of these blue small eddies (ions) in the velocity axis is smaller than their counterpart in red (neutrals). Panel (C): Modeled spread of the eddies in the spectral space as a Gaussian profile, with the width being their respective velocity dispersions. The area below these Gaussians is scaled linearly with the size of eddy l, while the velocity dispersions of the red curve and blue curve are scaled with $\sigma_v \propto l^{1/3}$ and $\sigma_v \propto l$ to imitate the difference in turbulence energy spectrum. The final spectral line (solid line) is given by the collective contributions of these profiles from individual eddies. Panel (D): Mock VCSs of the spectral lines modeled in Panel (C). For neutrals, the intensity fluctuations are more widely spread in the velocity space, while for ions, the intensity fluctuations are more localized in the narrow band of the velocity channel because turbulence-driven AD would tend to dissipate energy in small eddies. For species with less energy in small eddies, the VCS of its spectral lines should therefore contain more power in large k_v space. By studying the behavior in the Fourier space, VCS recovers the statistical description of the turbulence spectrum.

resolving this dilemma. Specifically, Burkhart et al. (2015) performed two-fluid MHD simulations to study a turbulence energy cascade in both super-Alfvénic and sub-Alfvénic medium. Their simulations hint at the further dependence of the decoupling scale on the Alfvénic Mach number ($M_A = V/V_A$) of the simulation boxes.

We caution our readers that the turbulent-driven AD presented here should not be confused with turbulence-accelerated AD (Fatuzzo & Adams 2002; Zweibel 2015), which describes how turbulence helps redistribute the magnetic flux in star-forming clouds and reduces the gravitationally driven AD timescale.

3. Target Selection and Data Acquisition

We chose a molecular cloud in NGC 6334, where B-fields have been shown to lie close to the plane of sky and play a dynamically important role in regulating the cloud fragmentation (Li et al. 2015). Complementing this with the fact that the cloud is situated far from regions with stellar feedbacks (NGC 6334 I, IN, V), it is an ideal venue for us to scrutinize this phenomenon in closer detail. Additionally, this relatively diffuse cloud ($n(H) \sim 10^4 \, \text{cm}^{-3}$) ensures that our tracers (HCN $(4-3)$, HCO$^+(4-3)$) are optically thin (Section 6), and the observed line profiles are not broadened by the optical opacity (right panel of Figure 2).
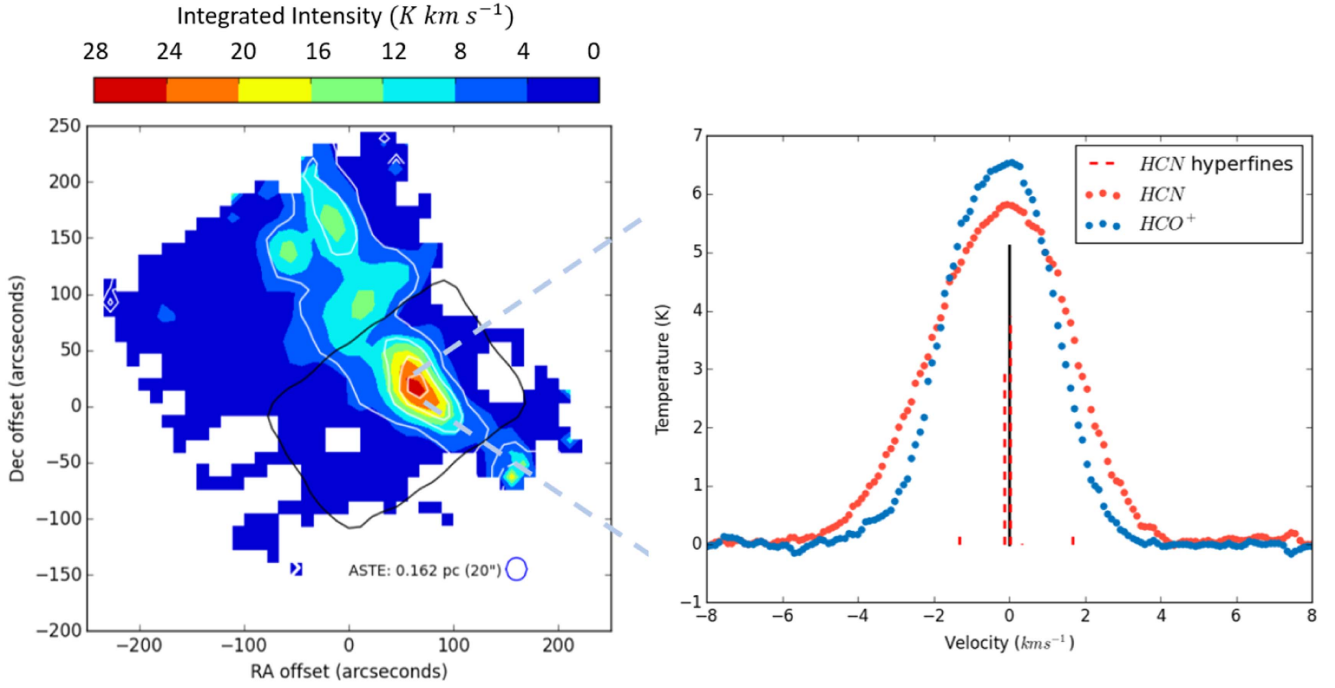
Figure 2. Left: Integrated intensity maps of HCN (white contours) and HCO$^+$ (colored plot) of this molecular cloud in NGC6334. The reference coordinate of this map is 17^h 20^m 36.8, −35°51′26″. The highest contour levels correspond to an integrated intensity of 20 K km s^{-1}; each following level is lowered by 5 K km s^{-1} accordingly. The color bar is in the scale of K km s^{-1}. The region adopted for VCS analysis is marked with a black line. Right: Spectral line profiles of both HCN and HCO$^+$ from the densest region show no signs of self-absorption. The relative intensities of HCN hyperfine lines assuming LTE (26) are plotted as dashed lines. The central and brightest component is shown as the gray solid line. The two brightest hyperfine satellites are only barely resolvable in our observations.

HCN(4 − 3) and HCO$^+$ are chosen as they are observed to be well correlated spatially in previous observations toward star-forming regions of different environments (e.g., Houde et al. 2000; Lo et al. 2009). The observations of this cloud were made with the Atacama Submillimeter Telescope Experiment (ASTE). With ASTE's 20″ resolution, the physical size of the achievable resolution is about 0.16 pc assuming that NGC 6334 is ~1.7 kpc away (Russeil et al. 2012). The left panel of Figure 2 shows the integrated intensity map of both HCN and HCO$^+$; the contour (HCN) and the color plot (HCO$^+$) are spatially highly correlated. This indicates that we compare neutrals and ions that trace a similar volume of the molecular clouds. For our carefully chosen cloud, neither the enhancement due to outflows nor the chemical evolution in proto-stellar cores would change the abundances of this neutral–ion pair conceivably (see Section 6).

4. Method: VCS

The VCS is defined as the power spectrum of the intensity fluctuations in the velocity coordinate along a fixed line of sight:

$$P_{\text{vcs}}(k_v) = |\int_{-\infty}^{\infty} I(v)e^{ik_v v}dv|^2, \qquad (2)$$

where $I(v)$ is the spectral line intensity at velocity v and k_v is the wavenumber in the velocity coordinate (i.e., $k_v = 2\pi/v$). The theoretical prediction of such a power spectrum is backed by the assumption of a power law-like energy spectrum for the turbulent velocity distribution, i.e., $E_v(k) \propto k^{-\kappa}$, and the density distribution, $E_\rho(k) \propto k^{-\gamma}$, where k corresponds to the wavenumber in spatial coordinates (i.e., $k = 2\pi/l$) and κ refers to the turbulence spectral index. For Kolmogorov-type

turbulence, the spectrum is expected to show a scaling of $\kappa = 5/3$. The full functional form of the VCS depends further on the temperature T, the VCS spectrum amplitude P_0, the noise level N_0, and the size of the cloud L,

$$P_{\text{vcs}}(k_v) = P_{\text{vcs}}(E_\rho(k), E_v(k), T, P_0, N_0, L). \qquad (3)$$

The non-trivial nature of the turbulent energy spectrum and its contribution to the intensity fluctuations along the velocity coordinate can be visualized using the schematic in Figures 1(B) and (C), which is inspired by Lazarian (2009), assuming three eddies of similar density but different velocity dispersion. The largest eddy would span the largest extent in the velocity axis, and therefore its contribution to the intensity fluctuations would be relatively evenly spread on the resulting spectral lines. On the other hand, the least energetic eddy would be localized in the velocity space and dominates the intensity fluctuations in the spectral lines. As a result of turbulence-driven AD, the small eddies of the ions should carry less turbulent energy than that of the neutrals and contribute its intensity across a narrower velocity range (Figure 1(B)). The ion spectral line is therefore expected to be more sharply peaked (Figure 1(C)). In the Fourier space, this translates into a shallower power spectrum (VCS) as the intensity fluctuations are predominantly concentrated in the larger k_v space (Figure 1(D)).

The power spectrum of HCN and HCO$^+$ (taken along the velocity axis) are first averaged over all the lines of sight to lower the noise. We focus our analyses toward the core region of this cloud (the region enclosed by the black contour in Figure 2), as other regions of this cloud have multiple density structures along their velocity axis. In light of the description of the schematic in Figure 1 and the simulation results from Meyer et al. (2014), Burkhart et al. (2015), and Li et al. (2012),

Table 1
Best-fit Turbulent Energy Spectrum per Unit Mass Returned from Fitting VCS to the Observed Power Spectrum of HCN and HCO$^+$

l	HCN	HCO$^+$
$l_{AD} < l < L$ $L = 1.26 \pm 0.11$ pc		$E(k) = (20.0 \pm 4.3)k^{-1.66\pm0.09}$ km^2 s^{-2} pc$^{1.66}$
$l < l_{AD}$ $l_{AD} = 0.404 \pm 0.132$ pc	same as above	$(49.7 \pm 13.6)k^{-2.01\pm0.05}$ km^2 s^{-2} pc$^{2.01}$

the turbulent spectrum of HCO$^+$ cannot be simply described by a single spectral index turbulent spectrum. Therefore, in our modeling of VCS, we have included one more spectral index κ_{AD} to describe the damping effect induced by magnetically driven AD for scales smaller than l_{AD} (i.e., $\kappa_{AD} > \kappa$). We should also note that in two-fluid turbulent MHD simulations, the transition of ions power spectrum from larger scale to the decoupling scale is usually smoother than in our broken power-law model (Li et al. 2012; Meyer et al. 2014; Burkhart et al. 2015). Even though it is simplified, our model captures the essential physics of the decoupling: the transition scale l_{AD} and the steep decay of turbulent energy in ions, while at the same time streamlining our fitting procedures. The detailed fitting procedures are outlined in Appendix A, where we also show that the temperature-dependent term and the density distribution term play a minor role in modifying the behavior of $P_{vcs}(k_v)$.

5. Results

The modeling of the VCS begins by first fitting the power spectrum of HCN, as it has fewer input parameters than HCO$^+$ and returns the information of the turbulent spectrum regarding larger scales (e.g., κ, L). These parameters are used in the further fitting of the spectrum of HCO$^+$ (e.g., l_{AD}, κ_{AD}). The resulting best-fit parameters and their respective standard deviation returned from the Scipy Optimize module and the error propagation are listed in Table 1.

5.1. Turbulent Spectra of Ions and Neutrals

The best-fit curve is shown together with the VCS of the two species in Figure 3. The best-fit parameters in Table 1 indicate that HCO$^+$ traces a steeper slope ($k^{-2.04}$) than that of HCN ($k^{-1.66}$) for $k > k_{AD}$. This corresponds to a steeper decay of the turbulent energy of the charged species and agrees with the theoretical prediction. The spectral index obtained for the neutral species is in agreement with ideal MHD simulations ($k^{-5/3}$ (Cho & Lazarian 2003)) and non-ideal simulations in the limit where R_M is large ($k^{-5/3}$ (Burkhart et al. 2015), $k^{-3/2}$ (Li et al. 2012)). Beyond the l_{AD}, simulations predicted a steeper decay (k^{-4} (Burkhart et al. 2015)) than what we observed. However, attention must be paid carefully to interpret simulation results as numerical viscosity would also damp the turbulent velocity structures at smaller scales. Higher-resolution simulations would be needed to confirm the results in the future.

5.2. Estimating the B-field

Following the recipe of Paper I, the plane of sky B-field strength can also be estimated with the decoupling scale l_{AD} and the turbulent energy spectrum by again setting the
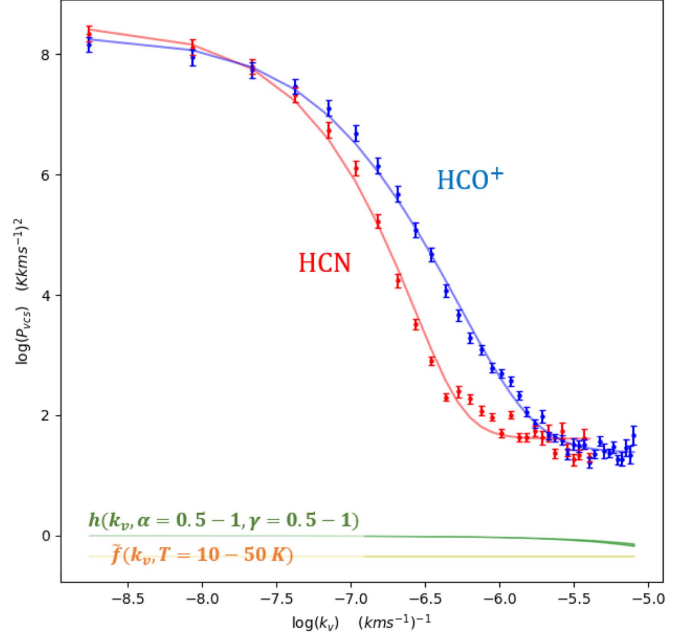

Figure 3. Power spectrum obtained for HCN and HCO$^+$ shown in log scale. The error bars correspond to one standard deviation in the scatter plot for HCN and HCO$^+$ (red and blue, respectively). The best fits returned from the fitting of VCS with these data are overlaid onto the data set as solid lines. The effects of both hyperfine structures and the gas temperature enter as extra factors in addition to the VCS, i.e. $P(k_v) = h(k_v, \alpha, \gamma)f(k_v, T)P_{vcs\text{-fit}}(k_v)$ (see Appendix). Since Figure 3 is presented in log–log space, these extra factors would simply upshift/downshift our best-fit VCS. The green line demonstrates how the inclusion of the two brightest and most probable hyperfine structures $h(k_v, \alpha, \gamma)$ would affect the behavior of VCS for α and γ that ranges from 0.5 to 1, where α and γ are the exaggerated relative intensities of these hyperfine satellites to the main line. The yellow line demonstrates the effect of the temperature-dependent term $f(k_v, T)$ for temperatures ranging from $T = 10$–50 K. It is nevertheless clear that both temperature and hyperfine satellite would contribute only when large k_v is considered.

magnetic Reynold number to one:

$$B = 0.316 \text{ mG} \left(\frac{l_{AD}}{0.5\text{pc}}\right)^{\frac{1}{2}} \left(\frac{V_n}{1 \text{ km s}^{-1}}\right)^{\frac{1}{2}} \left(\frac{n_n}{10^4 \text{ cm}^{-3}}\right) \left(\frac{\chi_i}{10^{-7}}\right)^{\frac{1}{2}},$$
(4)

where V_n is the velocity dispersion that corresponds to eddies at the decoupling scale l_{AD}. V_n can be estimated by multiplying the energy spectrum with the spread of turbulent eddies in the spectral space Δk, i.e., $V_n \approx \sqrt{E(k)\Delta k}$. Assuming that a turbulent eddy of size l is normally distributed on the spatial axis with a FWHM of L, the corresponding spread in the spectral space would be $\Delta k = \sqrt{8\ln 2/l}$ (Paper I). This gives $V(l_{AD}) \sim 1.11 \pm 0.27$ km s^{-1}. A recent analysis of the cloud in NGC 6334 was performed with a combination of multi-wavelength dust continuum measurements (André et al. 2016). A column density of 0.7–1 $\times$ 10^{23} cm^{-2} is estimated for this

cloud. This gives an average density $n(\mathrm{H_2}) \approx (2.19 \pm 0.32) \times 10^4\,\mathrm{cm^{-3}}$ with our estimated line-of-sight scale $L \approx 1.26$ pc. For $n_\mathrm{n} \approx 10^4\,\mathrm{cm^{-3}}$, the ionization fraction is approximately 10^{-7} for an assumed cosmic-ray ionization rate of $\approx 10^{-16}\,\mathrm{s^{-1}}$ (Draine 2011). Using these values, we arrive at an estimated B-field strength 0.665 ± 0.185 mG. We compared this estimate with the $B - n$ scaling relation $B = 0.19\,\mathrm{mG}(n/(10^3\,\mathrm{cm^{-3}}))^{0.41}$ from the same region (Li et al. 2015). For a number density of $n(\mathrm{H}) \sim 2.19 \times 10^4\,\mathrm{cm^{-3}}$, it predicts a B-field strength of 0.673 mG, which is close to our independent estimate.

6. Possible Effects of the Tracers on our Study

6.1. Relative Abundances between HCN and HCO^+

The chemical evolution of ions and neutrals in pre-stellar cores was studied (Tassis et al. 2012) and their simulations demonstrated that the variation in the abundance ratio between $\mathrm{HCN}/\mathrm{HCO^+}$ spans several orders of magnitude in almost all models with B-fields. However, the effects of turbulence are not included. In the presence of turbulent mixing, the relative abundance should vary to a lesser degree. $\mathrm{HCO^+}$ is shown to be more abundant at larger spatial scales that trace regions with a higher level of turbulence. In principle, this should give rise to a larger line width than the neutral species. This is contrary to observations (Paper I, Hezareh et al. 2010, 2014) as well as to the map we presented. In particular, at scales comparable to the size of the cores (≈ 0.1 pc), the radial dependence of the $\mathrm{HCN}/\mathrm{HCO^+}$ abundance ratio flattens out (Tassis et al. 2012). Our observation is incapable of resolving the core scale with a beam size of ~ 0.16 pc, and we therefore probe scales where the abundance ratio of HCN and $\mathrm{HCO^+}$ is roughly uniform. On the other hand, the abundances of $\mathrm{HCN}/\mathrm{HCO^+}$ are observed to be boosted in the presence of outflows. HCN traces the most energetic outflows, while $\mathrm{HCO^+}$ generally traces regions close to the base of the outflows (Walker-Smith et al. 2014). The former is reported to be more enhanced by a factor of ~ 10–100 times in the outflow linewings (Tafalla et al. 2010). However, the cloud we presented in our study is far away from the active star-forming region NGC 6334(I), (IN) and (V) with prominent stellar feedback. No detectable outflow has been reported in our region of interest.

6.2. Hyperfine Structures of HCN

The quadrupole moment induced by the nitrogen atom of HCN is responsible for its widely spaced hyperfine structures. For transitions from rotational level $J = 4 - 3$, there are five transitions based on the measurement of Ahrens et al. (2002). Assuming local thermal equilibrium condition, the two brightest satellite lines deviate from the main transition by $0.12\,\mathrm{km\,s^{-1}}$ and $0.038\,\mathrm{km\,s^{-1}}$, respectively. This offset cannot account for our observed σ difference between the two species ($\sim 0.4\,\mathrm{km\,s^{-1}}$).

The effect of hyperfine structures on the application of VCS is addressed here. We assume that the main line has the form of $I(v)$, then the spectral line with the inclusion of the two most probable satellite lines can be mimicked by

$$I_\mathrm{hyper}(v) = \alpha I(v - a) + I(v) + \gamma I(v + b), \qquad (5)$$

where α and γ are the relative peak intensity of the two satellite lines; a and b are the shift of the hyperfine satellites on the

frequency/velocity axis with respect to the main lines. The resulting power spectrum of the spectral lines in the presence of hyperfines would be in the form of

$$
\begin{aligned}
P_\mathrm{hyper}(k_v) &= |\int_{-\infty}^{\infty} I_\mathrm{hyper}(v) e^{ik_v v} dv|^2 \\
&= [1 + \alpha^2 + \gamma^2 + 2\alpha \cos(k_v a) + 2\gamma \cos(k_v b) \\
&\quad + 2\alpha\gamma \cos(k_v(a + b))] P_\mathrm{vcs}(k_v) \\
&= h(k_v, \alpha, \gamma) P_\mathrm{vcs}(k_v).
\end{aligned}
\tag{6}
$$

The resulting power spectrum has an additional factor that depends on k_v. The effect of including this extra factor $h(k_v, \alpha, \gamma)$ in the VCS is demonstrated in Figure 3. Since Figure 3 is presented in log–log space, the inclusion of $h(k_v, \alpha, \gamma)$ would simply upshift or downshift $P_\mathrm{VCS}(k_v)$ and will not change the shape of the VCS fitting. The hyperfine factor $h(k_v, \alpha, \gamma)$ stays rather uniform for the range of interest k_v and has minute effects on the modeling of VCS. Similarly, the temperature-dependent term can be factored out of the formula for VCS and varies insignificantly over the range of k_v concerned.

6.3. Optical Depths of the Tracers

We estimate the optical depth of the two tracers HCN and $\mathrm{HCO^+}$ with the online version of the code RADEX (van der Tak et al. 2007). $\mathrm{HCO^+}(3 - 2)$ data of NGC 6334 are best fit to the model of the cloud with a fractional abundance of $\mathrm{HCO^+}$ $X(\mathrm{HCO^+}) = 2 \times 10^{-9}$ (Zernickel et al. 2013). Assuming a column density of $N(\mathrm{H}) \approx 8.5 \times 10^{22}\,\mathrm{cm^{-2}}$ as above, this gives a column density of $N(\mathrm{HCO^+}) \approx 1.7 \times 10^{14}\,\mathrm{cm^{-2}}$. For the $(4 - 3)$ transition, $\mathrm{HCO^+}$ is marginally optically thin with an optical depth of 0.86. Although there are no existing measurements of HCN abundances in this particular cloud, we can estimate the $N(\mathrm{HCN})$ with the abundance ratio between HCN and $\mathrm{HCO^+}$ found in general star-forming regions ($N(\mathrm{HCN})/N(\mathrm{HCO^+}) \approx 2$; Godard et al. 2010). This gives an HCN optical depth of 0.127, which again is optical thin. A more detail discussion of the effect of the optical depth on the VCS is given in Lazarian & Pogosyan (2006). They suggested that absorption will tend to diminish the correlation between the intensity of emissions at widely separated velocities and line-of-sight scales. They also provide the velocity range v for the application of the VCS, which is $v < V_\mathrm{abs} \approx V(L)/\tau$ (we rearranged Equation (72) in Lazarian & Pogosyan (2008); τ is the optical depth of the tracer, and V_abs is the upper velocity limit set by the effect of absorption). A more sophisticated treatment for self-absorbed lines is given in Lazarian & Pogosyan (2008). In our particular case, HCN will be optically thinner than $\mathrm{HCO^+}$. This means that HCN is better at tracing the entire range of turbulent spectrum and will therefore place a good constraint on the input turbulent spectrum for the modeling of $\mathrm{HCO^+}$. As long as the velocity scale at l_AD, $V(l_\mathrm{AD})$ is smaller than V_abs, our result will still hold.

7. Improvement over Previous Studies

As a demonstration, we apply the same technique as employed in Paper I to our data set and discuss its applicability. The measure of velocity dispersion versus size is an important way to characterize the turbulence in molecular clouds. In order to study the hierarchical turbulent structures, Ostriker et al. (2001)
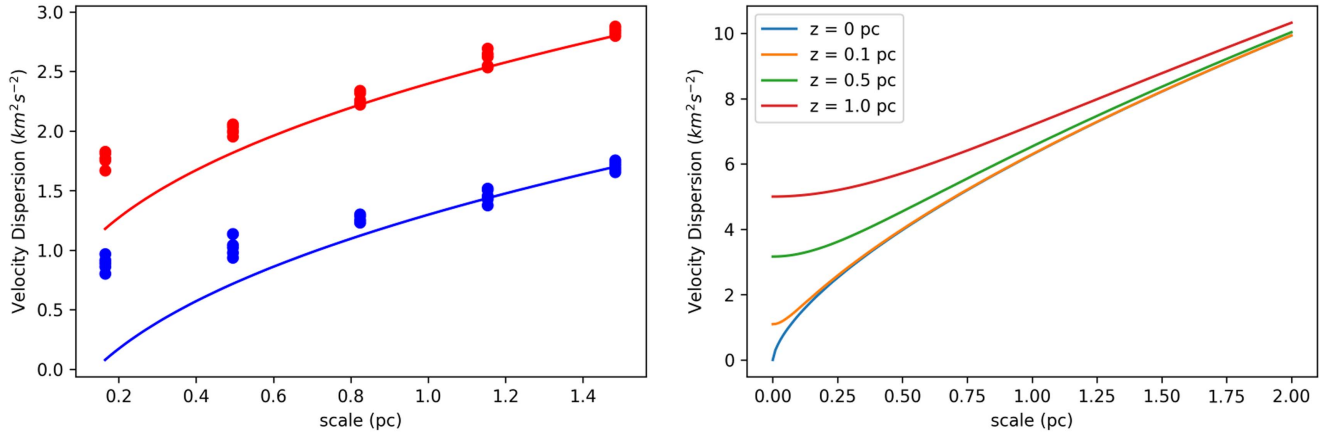
Figure 4. Left panel: Lower envelope of the squared velocity dispersion of HCN and HCO$^+$, shown in red and blue, respectively, as a function of the beam size R. Our best fit of the lower envelope is presented in Equation (7). Right panel: Dependence of σ^2 as a function of the beam size R on the line-of-sight scale z, $\sigma^2 \propto (\sqrt{(2R)^2 + z^2})^m$. As the beam R size decreases, the observed velocity dispersion σ^2 saturates at z^m. This lower envelope technique might not recover the turbulent spectrum well for scales smaller than the line-of-sight depth.

coarse-grained their simulated spectral data cubes to different resolutions/beam sizes and measured the velocity dispersions along all the lines of sight as a function of scale, as in Figure 4. They showed that the underlying turbulent velocity spectrum can be well recovered by fitting the lower envelope of such velocity dispersion distributions. This method relies on the idea that the lower envelope of the σ^2 distribution traces regions that sample the shortest lines of sight, such that the change in the beam size dominates the variation in the measured σ^2. This technique was studied further in detail by Falceta-Gonçalves et al. (2010). They showed that this technique only marginally recovered the actual dispersion in the marginally supersonic case (see Figure 2 of Falceta-Gonçalves et al. 2010). Furthermore, they showed that in highly supersonic simulations, the lower envelope of such a velocity dispersion distribution will underestimate the actual velocity dispersion as a function of scale. This can be understood with the fact that supersonic turbulence can easily induce a high-density contrast. The resulting distribution is therefore biased to denser regions and less susceptible to the velocity distribution. This renders the application of this method to observational data problematic.

We first sample the lower envelope of σ^2 of HCN as a function of (synthetic) beam size, and locate the pointing where HCN samples the shortest line of sight. We then compare the σ^2 of HCO$^+$ from these locations. The lower envelope of HCN can be well described by a power-law fitting for $R \geqslant 0.3$ pc, as shown in Figure 4,

$$\sigma_{\mathrm{HCN}}(R)^2 = 2.99 \left(\frac{R}{1\mathrm{pc}} \right)^{0.393} \mathrm{km}^2\,\mathrm{s}^{-2}$$

$$\sigma_{\mathrm{HCO}^+}(R)^2 = 2.99 \left(\frac{R}{1\mathrm{pc}} \right)^{0.393} - 1.05\,\mathrm{km}^2\,\mathrm{s}^{-2}. \quad (7)$$

We interpret the deviation of the σ^2 at $R \leqslant 0.5$ pc for both HCN/HCO$^+$ as the saturation of the σ^2 when the beam size falls below the line-of-sight scale. Here we demonstrate the effect of the line-of-sight depth on the measured σ^2 in Figure 5 with a simple model $\sigma^2 \propto (\sqrt{2R^2 + z^2})^m$, with R being the beam size, z being the line-of-sight depth, and m being the scaling exponent of turbulence. When the line-of-sight depth

$z = 0$ pc, the variation of σ^2 is dominated by the change in beam size. This is the ideal scenario where this lower envelope method works best. For models with $z > 0$ pc, when the beam size $R \leqslant z$, σ^2 only settles on the lower limit set by the line-of-sight scale z. The scaling of σ^2 recovers the trend traced by the blue lines for the beam size with $R \geqslant z$.

Figure 5 might also explain why the slopes inferred from this method to observation data ($m \approx 0.36$ (Paper I), $m \approx 0.3$–0.52 (Hezareh et al. 2010, 2014)), are consistently shallower than the expected scaling (Kolmogorov turbulence: $m = 2/3$; compressible turbulence: $m = 1$; the result from the work with VCS: $m \approx 0.65$)). Considering scales where $R \approx z$, the slope/scaling inferred from this plot is always shallower than the actual spectral index. As observers for most of the time have no accurate information about the line-of-sight depths, it is hard to determine which regime we are in. Moreover, the inhomogeneous density structures along the line of sight could also affect the line shape or line width. The result of our simplified model assuming homogeneous density distribution indeed resembles the prediction in the subsonic simulations (see Figure 2 of Falceta-Gonçalves et al. (2010)).

Here we also experiment with the fitting of the lower envelope accounting for the contributions from the finite line-of-sight depth with the scaling index, $m = 0.65$ derived from the fixed VCS (Figure 5). This allows us to estimate the line-of-sight depth of these two tracers,

$$\sigma_{\mathrm{HCN}}^2(R, z_{\mathrm{HCN}}) = C(\sqrt{2R^2 + z_{\mathrm{HCN}}^2})^{0.65}$$

$$\sigma_{\mathrm{HCO}^+}^2(R, z_{\mathrm{HCO}^+}) = C(\sqrt{2R^2 + z_{\mathrm{HCO}^+}^2})^{0.65} - D. \quad (8)$$

Free parameters for the fitting and the respective best-fit parameters are shown in Table 2. The fitting shows that the line-of-sight depth estimate $z_{\mathrm{HCN}} \approx 1.12 \pm 0.07$ pc is consistent with the cloud scale $L \approx 1.26 \pm 0.11$ pc we derived with the VCS. This reinforces our explanation of the saturation of the velocity dispersion due to unresolved line-of-sight depths. Furthermore, we also find that z_{HCO^+} is larger than z_{HCN}. This is also consistent with the fact that HCO$^+$ has a lower critical density than HCN (Jansen 1995), and therefore is capable of exciting emission from a longer line-of-sight depth. This also
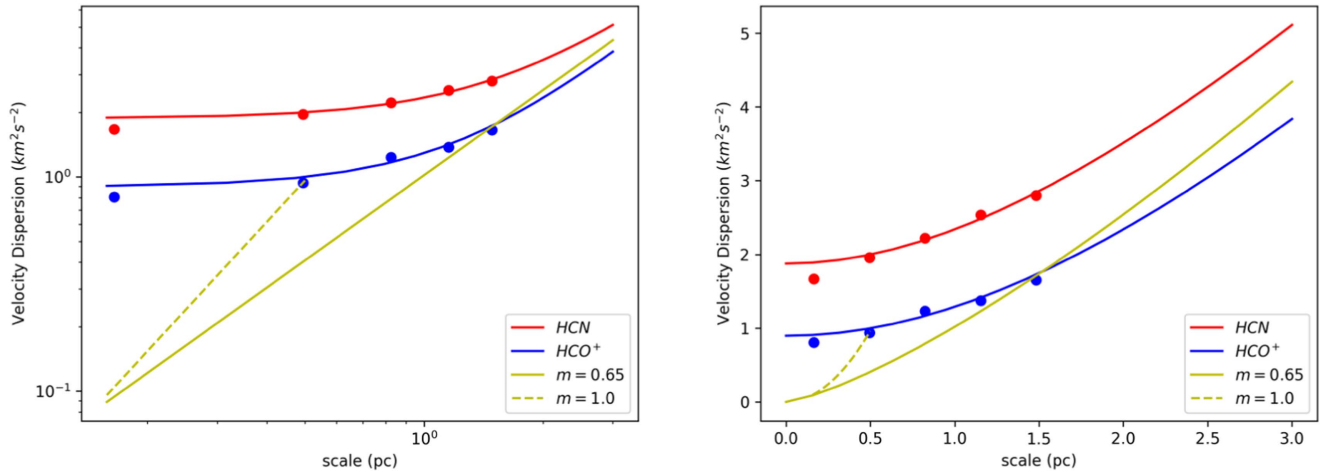
Figure 5. Lower envelope fitting accounting for the velocity dispersion contribution from the finite line of sight of the observed cloud in linear scale (left panel) and log–log scale (right panel). The filled dots show the lower envelope of the HCN (red) and HCO$^+$ (blue). The solid lines are the respective best fit from the lower envelope fitting. For reference, we also show here the scaling we derived from VCS, i.e., $\sigma^2 \propto r^{0.655}$ (HCN) and $\sigma^2 \propto r^{1.04}$ (HCO$^+$).

Table 2
List of Parameters Derived from Fitting the Lower Envelope of Velocity
Dispersions Accounting for the Finite Line-of-sight Depth

z_{HCN}	1.12 ± 0.07 pc
z_{HCO^+}	1.48 ± 0.35 pc
C	1.61 ± 0.09 km^2 s^{-2} pc$^{-1.3}$
D	1.80 ± 0.8 km^2 s^{-2}

explains the larger spatial extent of HCO$^+$ compared to that of HCN observed in this work (Figure 2, left panel) and possibly observations in general star-forming regions (Paper I; Houde et al. 2000; Lo et al. 2009; Hezareh et al. 2014). The estimation of the line-of-sight depth enables us to infer the three-dimensional morphology of this particular molecular cloud. Since the line-of-sight depth is comparable to the plane-of-sky scale, this hints at a flattened cloud core geometry (with dimensions of 1 pc width × 1 pc depth × 0.5 pc height). This is a signature of anisotropic collapse induced by dynamically important B-fields since the magnetic force is only perpendicular to the field lines. The non-spherical nature of star-forming cores has been studied extensively by Tritsis et al. (2015) with observation data.

We also examine the sensitivity of the VCS fit of HCO$^+$ to the change in z_{HCO^+}. In the previous section, we adopt the best-fit cloud scale of HCN as that of HCO$^+$. This might be oversimplifying as HCO$^+$ is expected to trace a longer line of sight. We repeat the fitting of VCS for HCO$^+$ by replacing L with $z_{HCO^+} \approx 1.48$ pc. The optimal fitting gives an $l_{AD} \approx 0.547 \pm 0.213$ pc and is still in agreement with the result we reported, $l_{AD} \approx 0.404 \pm 0.132$ pc.

8. Implication of this Study

8.1. Validity of Chandraskhar–Fermi Method on Sub-parsec Scales

Chandrasekhar and Fermi (Chandrasekhar & Fermi 1953) proposed a method for measuring the B-field strength by assuming the equipartition between turbulent kinetic energy (velocity dispersion) and turbulent B-field energy, which is inferred from thermal dust polarization (hereafter C–F method). However, this assumption might break down for scales

$L \lesssim l_{AD}$, when the B-field decouples from bulk gas flows. Indeed, simulations have shown that the deviation of the estimate with the C–F method with the actual B-field strength increases as the magnetic Reynolds number decreases (Li et al. 2012). Specifically, the C–F method will overestimate the actual B-field strength. The C–F method therefore should be applied with care depending on the physical conditions of the molecular clouds.

8.2. Possible Resolution to the Magnetic Braking Catastrophe

The mechanism behind proto-stellar disk formation is still a matter of debate, and turbulence has been proposed to be the source of the angular momentum (e.g., Seifried et al. 2012). The B-field directions from cloud cores at the 0.1 pc scale and their surrounding intercloud medium at 100 pc scale are found to be well aligned (Li et al. 2009). Recently, this signature of dynamically dominant B-fields has also been observed down to 0.01 pc (Li et al. 2015). Whether the situation extends to the scales of proto-stellar disk formation is unknown, but a recent simulation presented by Zhang et al. (2018, submitted) suggested that dense cores that formed out of an initially sub-Alfvénic parent cloud cannot be highly super-Alfvénic. In other words, turbulent eddies may not be energetic enough to drive disk rotation against magnetic forces. The lack of an effective energy supply to overcome B-fields and form disks is called magnetic braking catastrophe. The observation of l_{AD} at sub-parsec scales may shed light on this catastrophe. With the canonical ionization equilibrium $n_i \propto n_n^{1/2}$ (Draine 2011) and a constant drag coefficient between ions and neutrals γ_d, the magnetic Reynolds number $R_M \propto (n_i n_n lV)/B^2$ should scale roughly to $R_M \propto l^{0.1-0.9}$, which decreases monotonically as one progresses to even smaller scales. If turbulence-driven AD is at work already at sub-parsec scales as presented, a high degree of decoupling between turbulent eddies and the B-fields is expected for disk forming kau (~ 1000 au) scales. This also implies that disks with angular momentum that stems from local turbulent eddies within the decoupling scale need not be aligned with the local B-field (Hull et al. 2014), which is usually expected in the strong-field scenario where flux freezing is assumed.

9. Conclusion

Building upon the foundations laid in Paper I, we present a new recipe to model turbulent AD and apply it to a diffuse quiescent molecular cloud in NGC6334. With VCS, we model the turbulent energy spectrum of both ions and neutrals with HCN and HCO$^+$(4 − 3) spectral lines. We show that the result is best understood with a break in the ions' turbulent spectrum at $l_{AD} = 0.404 \pm 0.132$ pc. This is consistent with the theory put forward in Paper I that the disturbances in B-fields are damped by turbulence-driven AD. We argue that our result is unlikely to be artifacts from tracer properties, chemistries, or optical depths. Moreover, we show that the method adopted in this work can circumvent the effect of the unresolved line-of-sight depth of the tracers and is better at tracing the actual turbulent spectrum than the technique used in previous works. The discovery of turbulence-driven AD that operates at the sub-parsec scale is important, as this challenges the applicability of the CF method at the molecular cloud core scale, and it might shed light on the magnetic braking catastrophe in the theory of proto-stellar disk formation. More observations would be essential to determine whether this is a general process in molecular cloud cores and to constrain its role in the context of star formation.

Appendix A
The Fitting of the VCS

The VCS technique is based on the study of the intensity fluctuations/spectral lines along the velocity axis. The theoretical prediction of this power spectrum relies on the assumption of a power law-like spectrum for both turbulent velocity and the density distribution. The VCS is defined to be the power spectrum of the intensity fluctuations in the velocity coordinate along a fixed line of sight:

$$P_{vcs}(k_v) = |\int_{-\infty}^{\infty} I(v)e^{ik_v v}dv|^2, \qquad (9)$$

where I_v is the spectral line intensity at velocity v and k_v is the wavenumber in the velocity coordinate (e.g., $k_v = 2\pi/v$). The expression of the VCS is of the following form (Chepurnov et al. 2015):

$$P_{vcs}(k_v) = f^2(k_v)P_0 \int d^3\boldsymbol{r} \quad C_\epsilon(\boldsymbol{r})g(\boldsymbol{r})d\boldsymbol{r}e^{-k_v^2/2D_{vz}(\boldsymbol{r})} + N_0, \qquad (10)$$

where f is the Fourier transform of the Maxwellian distribution, which depends on temperature, P_0 is the spectrum amplitude, $C_\epsilon(\boldsymbol{r})$ is the density correlation function, $g(\boldsymbol{r})$ is the geometric factor that accounts for the beam pattern and structures along
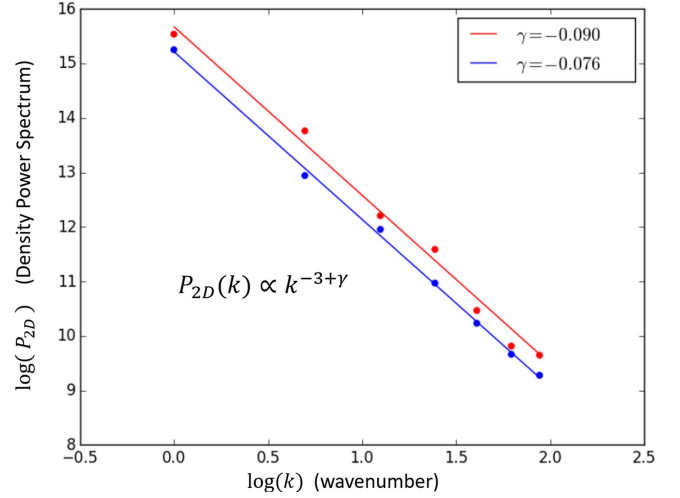

Figure 6. Two-dimensional column density power spectrum of HCN and HCO$^+$ in log–log scale. $\gamma < 0$ corresponds to a steep density power spectrum. The density correlation function C_ϵ can be factored out from the integration of the VCS. This simplifies the fitting procedures.

the line of sight, $D_{vz}(\boldsymbol{r})$ is the structure function of the turbulent velocity component along the line of sight, and N_0 is a constant that depends on the noise level.

The temperature-dependent term f and the density correlation function term C_ϵ can be determined independently before fitting the VCS. The temperature of this cloud is on the order 20–30 K (André et al. 2016). This translates into a thermal velocity of 0.1 km s^{-1} for both HCN and HCO$^+$. In Figure 3, it is clear that $f^2(k_v, T)$ has a weak functional dependence on k_v in the range in which we fit our model. The density correlation function can be derived from the study of the two-dimensional spatial power spectrum of the column density map (Lazarian & Pogosyan 2000). The power spectrum would be in the form of $P_{2D}(k) \propto k^{-3+\gamma}$. The density correlation function is steep when $\gamma < 0$ and shallow when $\gamma > 0$. The contribution of the density fluctuations has a weak dependence on the VCS when the density correlation function is steep (Lazarian & Pogosyan 2006). Here we showed the spatial power spectrum of the column density map for both HCN and HCO$^+$ in Figure 6. These two species showed almost an identical trend, which is again an indication of the high correlation between the two species. Since $\gamma < 0$ for both species, the density correlation term $C_\epsilon(\boldsymbol{r})$ can be factored out from the integration that follows.

In the optically thin limit, VCS can now take a simpler form,

$$P_{vcs}(k_v) = P_0 \int d^3\boldsymbol{r} \quad g(\boldsymbol{r})e^{-k_v^2/2D_{vz}(\boldsymbol{r})} + N_0. \qquad (11)$$

The free parameters needed to model the VCS reduce to P_0, N_0, $D_{vz}(\boldsymbol{r}) = \langle(v_z(\boldsymbol{x}) - v_z(\boldsymbol{x} + \boldsymbol{r}))^2\rangle$. The structure function $D_v(r)$ and the turbulent energy spectrum can be converted from one into the other through a Fourier transform.

For Komolgorov-type turbulence, the spectral index κ is given by 5/3. An extra spectral index κ_{AD} is introduced for the charged species to account for the dissipation of turbulent energy. However, when the line-of-sight scale z is no longer comparable to the plane-of-sky scale, the structure functions of the turbulent velocity component $D_{vz}(r, z)$ along the line of sight (Lazarian & Pogosyan 2006) for ions and neutrals are more complicated and are shown in Table 3. The term Cr^m accounts for the scaling of the velocity dispersion V of eddies

Table 3
Structure Function $D_{vz}(r, z)$ for HCN and HCO$^+$, Respectively

	$0 \leqslant r \leqslant l_{AD}$	$r \geqslant l_{AD}$
HCN	$Cr^m\left(1 + \frac{m}{2}\left(1 - \frac{z^2}{r^2}\right)\right)$	$Cr^m\left(1 + \frac{m}{2}\left(1 - \frac{z^2}{r^2}\right)\right)$
HCO$^+$	$C_{AD}r^{m_{AD}}\left[1 + \frac{m}{2}\left(1 - \frac{z^2}{r^2}\right)\right]$	$F + Cr^m\left[1 + \frac{m}{2}\left(1 - \frac{z^2}{r^2}\right)\right]$

of sizes r, while the term $[1 + m/2(1 - z^2/r^2)]$ accounts for the projection of velocity components onto the line-of-sight direction. The turbulent spectral index κ and κ_{AD} can be inferred from m and m_{AD} above with $\kappa = m + 1$ and $\kappa_{AD} = m_{AD} + 1$, respectively. C_{AD} and F are set by the boundary condition imposed by the continuity of the turbulent energy spectrum at the scale l_{AD} for a given C, m, m_{AD}

$$C_{AD} = m/m_{AD} \quad Cl_{AD}{}^{m-m_{AD}}$$
$$F = (m - m_{AD})/m_{AD} \quad Cl_{AD}{}^m. \quad (12)$$

The VCS of the observed spectral data cube are first obtained by taking the power spectrum of the spectral data cube along the velocity axis. The average of the VCS from all these different lines of sight is then taken so as to beat down the noise, i.e., $P_{vcs}(k_v) = \frac{1}{N}\sum_{x,y}|\int_{-\infty}^{\infty} I(x, y, v)e^{ik_v v}dv|^2$ (where N is the number of independent lines of sight). Before fitting it to the VCS shown above, one also needs to determine whether the density distribution of the observed cloud is in the shallow or steep regime, as this affects the VCS fitting form. Parameters required for the fitting of VCS are listed in Table 4. The modeling of VCS begins by first fitting the power spectrum of HCN as it has fewer input parameters than HCO$^+$ and returns the information of the turbulent spectrum regarding larger scales (e.g., C, m, L). These parameters are used in the fitting of the spectrum of HCO$^+$. The resulting best-fit parameters and their respective one standard deviation error returned from the Scipy Optimize module are listed in Table 5.

Appendix B
Would HCN be Better Explained by a Broken Power Law?

Ideally, when we fit the VCS to our result, we should not assume an underlying form of turbulent spectra a priori for either species. However, our current implementation of the VCS is incapable of fitting a more generalized form of turbulent spectra, i.e., including simultaneously the large-scale turbulent spectrum, the break scale, and the spectral index beyond the break.

In this section, we will test the robustness of the assumption of our single power-law turbulent spectrum for HCN. This is essential as the result constraints the input for fitting HCO$^+$. We fit the VCS of HCN for a range of dissipation scales l_{dis} assuming the initial HCN best-fit large-scale turbulent spectrum as shown in Table 5. If a single power-law turbulent spectrum is favored, the spectral index beyond the assigned break would be close to the initial large-scale power-law spectrum. The results are shown in Figure 7. The red dots are the best-fit scaling index for the assumed l_{dis} and are almost identical to our initial large-scale spectrum. This verifies our assumption of a single power-law turbulence spectrum for HCN. We show the same experiment result with HCO$^+$ as well. The results clearly favors the explanation with a steep turbulent spectrum for HCO$^+$.

Table 4
Input Parameters for Fitting the VCS to the Power Spectrum of HCN and HCO$^+$

	HCN	HCO$^+$
Spectrum Amplitude	P_0	P_1
Constant (noise)	N_0	N_1
Spectral Index $l \geqslant l_{AD}$	m	m
Velocity Dispersion	C	C
Size of the Cloud	L	L
Spectral Index $l \leqslant l_{AD}$	...	m_{dis}
Decoupling Scale	...	l_{AD}

Note. The boldface parameters are the free fitting parameters. The fitting of HCO$^+$ is followed by the modeling of HCN.

Table 5
Best-fit Result Returned from Fitting the VCS to the Power Spectrum of HCN and HCO$^+$

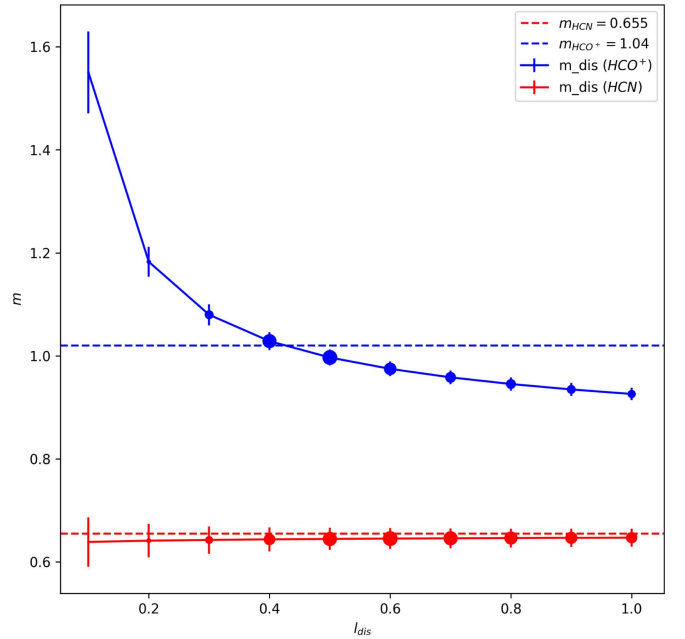|	HCN		HCO$^+$
C	9.16 ± 1.47 km^2 s^{-2}	m_{dis}	1.01 ± 0.049
m	0.655 ± 0.0935	l_{AD}	0.484 ± 0.158 pc
L_{cut}	1.26 ± 0.112 pc	C_{dis}	7.69 ± 2.07 km^2 s^{-2}
		D	2.0 ± 1.35 km^s s^{-2}

Figure 7. If HCN is better fit by a broken turbulent power law as in HCO$^+$, the best-fit spectral index beyond the break would deviate significantly from the initial best fit. The results are shown above in red. It is clear that they are close to the initial spectral index. The best-fit spectral index for HCO$^+$ is shown for comparison as well. The diameter of the marker is scaled inversely with the root mean squared error between the best-fit VCS and the actual data, i.e., the larger the marker size, the smaller the root mean squared error, and the better the fitting. This supports our claims that HCN is better fit with a power law-like turbulent spectrum without a break.

Appendix C
The Effect of Noise and Resolution on the VCS

The VCS is the power spectrum of the observed spectral lines. We can qualitatively understand the effect of noise on the observed spectrum by adding an additional noise term to the true signal. Here we introduce $N(v)$ to mimic the actual

observations across the velocity channel. Since $N(v)$ should be uncorrelated with the signal, its cross-integral with the actual signal would therefore vanish. The composite VCS would be left with two terms: the VCS of the clean signal, and the power spectrum of the noise term. We assume that the noise term is Gaussian distributed with a zero mean and a dispersion of $\langle |N(v)|^2 \rangle = N_0$. By Parseval's theorem, $\langle |N(k_v)|^2 \rangle = N_0$. Effectively, the noise term would introduce a baseline on the VCS spectrum. As soon as $P_{vcs}(k_v)$ is comparable to N_0, the VCS spectrum would be buried by the noise term and hence the range available for the fitting would be reduced. Both the VCS for ions and neutrals shown in Figure 3 flatten off to constant value at high k_v. This reinforces our assumption of a constant noise power spectrum. The effect of noise enters explicitly in the fitting function through the term N_0 defined in Table 4,

$$
\begin{aligned}
P_{vcs,noise}(k_v) &= |\int_{-\infty}^{\infty} (I(v) + N(v))e^{ik_v v} dv|^2 \\
&= \int_{-\infty}^{\infty} I(v_1)I(v_2)e^{ik_v(v_1-v_2)} dv_1 dv_2 \\
&\quad + \int_{-\infty}^{\infty} N(v_1)N(v_2)e^{ik_v(v_1-v_2)} dv_1 dv_2 \\
&\quad + 2\int_{-\infty}^{\infty} I(v_1)N(v_2)e^{ik_v(v_1-v_2)} dv_1 dv_2 \\
&= P_{vcs}(k_v) + \langle N(k_v)^2 \rangle \\
&= P_{vcs}(k_v) + N_0.
\end{aligned}
\tag{13}
$$

In the model of the VCS, the size of telescope beam is handled explicitly through the geometric factor $g(r)$ (Chepurnov et al. 2010). Chepurnov et al. (2010) and Chepurnov et al. (2015) showed that the fitting of the VCS on the same data with different resolutions gives the same fitting results on the turbulent spectra by changing only the geometric factor. This shows the robustness of the techniques to the effect of spatial resolution. In reality, the spatial resolution limits the number of independent line-of-sight spectra and increases the error bar of the VCS inferred from the data.

ORCID iDs

Kwok Sun Tang ⓘ https://orcid.org/0000-0003-1902-1680
Hua-Bai Li ⓘ https://orcid.org/0000-0003-2641-9240
Wing-Kit Lee ⓘ https://orcid.org/0000-0002-5319-3673

References

Ahrens, V., Lewen, F., Takano, S., et al. 2002, ZNatA, 57, 669
André, P., Revéret, V., Könyves, V., et al. 2016, arXiv:1605.07434
Balsara, D. S. 1996, ApJ, 465, 775
Burkhart, B., Lazarian, A., Balsara, D., Meyer, C., & Cho, J. 2015, ApJ, 805, 118
Chandrasekhar, S., & Fermi, E. 1953, ApJ, 118, 113
Chepurnov, A., Burkhart, B., Lazarian, A., & Stanimirovic, S. 2015, ApJ, 810, 33
Chepurnov, A., Lazarian, A., Stanimirović, S., Heiles, C., & Peek, J. E. G. 2010, ApJ, 714, 1398
Cho, J., & Lazarian, A. 2003, MNRAS, 345, 325
Crutcher, R. M., Wandelt, B., Heiles, C., Falgarone, E., & Troland, T. H. 2010, ApJ, 725, 466
Draine, B. T. 2011, Physics of the Interstellar and Intergalactic Medium (Princeton, NJ: Princeton Univ. Press)
Falceta-Gonçalves, D., Lazarian, A., & Houde, M. 2010, ApJ, 713, 1376
Fatuzzo, M., & Adams, F. C. 2002, ApJ, 570, 210
Godard, B., Falgarone, E., Gerin, M., Hily-Blant, P., & de Luca, M. 2010, A&A, 520, A20
Heyer, M. H., & Brunt, C. M. 2004, ApJL, 615, L45
Hezareh, T., Csengeri, T., Houde, M., Herpin, F., & Bontemps, S. 2014, MNRAS, 438, 663
Hezareh, T., Houde, M., McCoey, C., & Li, H.-b. 2010, ApJ, 720, 603
Houde, M., Bastien, P., Peng, R., Phillips, T. G., & Yoshida, H. 2000, ApJ, 536, 857
Hull, C. L. H., Plambeck, R. L., Kwon, W., et al. 2014, ApJS, 213, 13
Jansen, D. J. 1995, PhD thesis, Leiden Observatory, Leiden Univ.
Jiang, H., Li, H-B., & Fan, X. 2018, ApJ, submitted
Lazarian, A. 2009, SSRv, 143, 357
Lazarian, A., & Pogosyan, D. 2000, ApJ, 537, 720
Lazarian, A., & Pogosyan, D. 2006, ApJ, 652, 1348
Lazarian, A., & Pogosyan, D. 2008, ApJ, 686, 350
Li, H.-b., Dowell, C. D., Goodman, A., Hildebrand, R., & Novak, G. 2009, ApJ, 704, 891
Li, H.-B., Goodman, A., Sridharan, T. K., et al. 2014, in Protostars and Planets VI, ed. H. Beuther et al. (Tucson, AZ: Univ. Arizona Press), 101
Li, H.-B., & Houde, M. 2008, ApJ, 677, 1151
Li, H.-B., Houde, M., Lai, S.-p., & Sridharan, T. K. 2010, ApJ, 718, 905
Li, H.-B., Yuen, K. H., Otto, F., et al. 2015, Natur, 520, 518
Li, P. S., McKee, C. F., & Klein, R. I. 2012, ApJ, 744, 73
Lo, N., Cunningham, M. R., Jones, P. A., et al. 2009, MNRAS, 395, 1021
McKee, C. F., & Ostriker, E. C. 2007, ARA&A, 45, 565
Mestel, L., & Spitzer, L., Jr. 1956, MNRAS, 116, 503
Meyer, C. D., Balsara, D. S., Burkhart, B., & Lazarian, A. 2014, MNRAS, 439, 2197
Mouschovias, T. C. 1979, ApJ, 228, 475
Mouschovias, T. C. 1987, in NATO ASIC Proc. 210, Physical Processes in Interstellar Clouds, ed. G. E. Morfill & M. Scholer (Dordrecht: Reidel), 453
Mouschovias, T. C. 1991, ApJ, 373, 169
Mouschovias, T. C., Ciolek, G. E., & Morton, S. A. 2011, MNRAS, 415, 1751
Mouschovias, T. C., & Tassis, K. 2010, MNRAS, 409, 801
Nakano, T., Nishi, R., & Umebayashi, T. 2002, ApJ, 573, 199
Oishi, J. S., & Mac Low, M.-M. 2006, ApJ, 638, 281
Ostriker, E. C., Stone, J. M., & Gammie, C. F. 2001, ApJ, 546, 980
Padoan, P., Juvela, M., Kritsuk, A., & Norman, M. L. 2009, ApJL, 707, L153
Russeil, D., Zavagno, A., Adami, C., et al. 2012, A&A, 538, A142
Seifried, D., Banerjee, R., Pudritz, R. E., & Klessen, R. S. 2012, MNRAS, 423, L40
Tafalla, M., Santiago-García, J., Hacar, A., & Bachiller, R. 2010, A&A, 522, A91
Tassis, K., Hezareh, T., & Willacy, K. 2012, ApJ, 760, 57
Tilley, D. A., & Balsara, D. S. 2010, MNRAS, 406, 1201
Tritsis, A., Panopoulou, G. V., Mouschovias, T. C., Tassis, K., & Pavlidou, V. 2015, MNRAS, 451, 4384
van der Tak, F. F. S., Black, J. H., Schöier, F. L., Jansen, D. J., & van Dishoeck, E. F. 2007, A&A, 468, 627
Walker-Smith, S. L., Richer, J. S., Buckle, J. V., Hatchell, J., & Drabek-Maunder, E. 2014, MNRAS, 440, 3568
Zernickel, A., Schilke, P., & Smith, R. J. 2013, A&A, 554, L2
Zhang, Y., Guo, Z., Wang, H. H., & Li, H.-B. 2018, ApJ, submitted
Zweibel, E. G. 2015, ASSL, 407, 285